International Journal on Recent and Innovation Trends in Computing and Communication
ISSN: 2321-8169 Volume: 11 Issue: 11s
DOI: https://doi.org/10.17762/ijritcc.v11i11s.8092
***Article Received:** 20 June 2023 **Revised:** 22 August 2023 **Accepted:** 08 September 2023*

A Probabilistic Adaptive Cerebral Cortex Segmentation Algorithm for Magnetic Resonance Human Head Scan Images

Sivanesan Rajangam[1], Kalavathi Palanisamy[2]
[1]Department of Computer Science and Applications
The Gandhigram Rural Institute (Deemed to be University)
Chinnalapatti- 624302, Tamilnadu, India
e-mail: rajangamsivanesan@gmail.com
[2]Department of Computer Science and Applications
The Gandhigram Rural Institute (Deemed to be University)
Chinnalapatti- 624302, Tamilnadu, India
e-mail:pkalavathi.gri@gmail.com

Abstract—The total efficiency of Magnetic Resonance Imaging (MRI) results in the need for human involvement in order to appropriately detect information contained in the image. Currently, there has been a surge in interest in automated algorithms that can more precisely divide medical image structures into substructures than prior attempts. Instant segregation of cerebral cortex width from MRI scanned images is difficult due to noise, Intensity Non-Uniformity (INU), Partial Volume Effects (PVE), MRI's low resolution, and the very complicated architecture of the cortical folds. In this paper, a Probabilistic Adaptive Cerebral Cortex Segmentation (PACCS) approach is proposed for segmenting brain areas of T1 weighted MRI of human head images. Skull Stripping (SS), Brain Hemisphere Segmentation (BHS) and CCS are the three primary processes in the suggested technique. In step 1, Non-Brain Cells (NBC) is eliminated by a Contour-Based Two-Stage Brain Extraction Method (CTS-BEM). Step 2 details a basic BHS technique for Curve Fitting (CF) detection in MRI human head images. The left and right hemispheres are divided using the discovered Mid-Sagittal Plane (MSP). At last, to enhance a probabilistic CCS structure with adjustments such as prior facts change to remove segmentation bias; the creation of express direct extent training; and a segmentation version based on a regionally various Gaussian Mixture Model- Hidden Markov Random Field – Expectation Maximization (GMM-HMRF-EM). The underlying partial extent categorization and its interplay with found image intensities are represented as a spatially correlated HMRF within the GMM-HMRF-EM method. The proposed GMM-HMRF method estimates HMRF parameters using the EM technique. Finally, the outcomes of segmentation are evaluated in terms of precision, recall, specificity, Jaccard Similarity (JS), and Dice Similarity (DS). The proposed method works better and more consistently than the present locally Varying MRF (LV-MRF), according to the experimental findings obtained by using the suggested GMM-HMRF-EM methodology to 18 individuals' brain images.

Keywords- MRI, HMRF, Mid-Sagittal Plane (MSP), GMM, Partial Volume Effect (PVE).

I. INTRODUCTION

Brain ailment has emerged as one of the maximum extreme risks to human fitness in latest years, making it essential to properly appoint medical exam and quantitative evaluation for the identification of brain disorders. A wide range of brain imaging modalities has been developed, with MRI being the most widely used due to its improved assessment of several brain tissues. Many MRI-based studies, such as statistical tissue extent evaluation, taint and lesion identification, and surgical planning, need segmenting the imaging brain volume into mass categories like Grey Matter (GM), White Matter (WM), and Cerebro-Spinal Fluid (CSF). Procedures for segregating brain MR images into GM, WM, and CSF have gotten a lot of attention as an outcome [1].

The MRI machine creates 3D volumetric records stated as a stack of 2D slices, and computer-assisted tools are required to discover the information provided in the brain layer several brain image functions such as volumetric examining, detection, preparing for surgical intervention, creation of anatomical fashions, 3-D visualization and inducement brain ailments like multiple sclerosis. Methods based on morphological procedures, edge detection, fuzzy c-means, and probabilistic models have been used to segment the brain into its many tissue types. Several image segmentation techniques use the EM algorithm to fit stochastic nonlinear process. These image segmentation methods based on EM were found to be among the most accurate and robust. Each class is represented as a normal distribution with exponential translation to make the skew column cumulative, and INU is expected to be provided for by a Gaussian distributed bias field model [3]. To create and locally

International Journal on Recent and Innovation Trends in Computing and Communication
ISSN: 2321-8169 Volume: 11 Issue: 11s
DOI: https://doi.org/10.17762/ijritcc.v11i11s.8092
***Article Received:** 20 June 2023 **Revised:** 22 August 2023 **Accepted:** 08 September 2023*

limit the segmentation, a spatial consistency model using an MRF, explicit description of the INU using radial basis function, and few previous expertise of brain anatomy were used. Because of problems such as INU, PVE, Noise, Image aberrations, poor resolution, and a considerable degree of natural fluctuation, the local intensity difference shows that the neighborhood intensity variation is inadequate to give an accurate segmentation of optimal networks [4].

Image segmentation, surface reconstruction, and depth inference are among problems that MRFs have been used to tackle. Much of its efficiency may be attributed to advanced algorithms like Iterated Conditional Configurations, as well as its consideration of "data fidelity" and "model smoothness." A voxel in an MRI may 'contain' a single kind of tissue or a mixture of other types, according to the PVE. Because of the limited spatial resolution of MRI, the PVE should only appear at tissue class borders and have a maximum effect width of 1 or 2 voxels across the boundaries. This is because the imaging technique uses a diffuse point spread function, which effectively blends the intensity of each voxel with that of many of its surroundings. When the blurring effect is combined with the PVE at tissue boundaries, the mixing effect of intensities from diverse tissue types appears in a greater region of the image, based on the strength and imaging quality. To overcome this constraint, many techniques have been devised that include spatial information into the segmentation process, resulting in spatially coherent and noise-resistant results [5].

In contrast to the tissue segmentation challenge, the PVE classification problem assigns a continuous vector to each voxel, whereas the latter provides a discrete label to each voxel. Apart than that, these two concerns are nearly identical. The HMRF model that results is equally applicable to the PVE classification problem, with the exception that the hidden random field is a set of continuous matrices rather than discrete labels. If the data is multi-spectral for homogeneity, the model will be equally valid for single-spectral data with slight changes to the Gaussian's functional form. Because spatial correlation can be effectively described in a parametric form using the HMRF [6], the GMM combined with the HMRF has attracted a lot of interest.

Over the last few years, various GMM-based methods for brain MR segmentation have received a lot of attention. Because the brain tissue density distribution may be properly estimated by a Gaussian distribution and the difference between distinct tissue classes is considerable, GMM provides a feasible probabilistic model for explaining the image intensities of different tissue classes. Furthermore, because GMM is a well-known model, implementing it using the EM technique is computationally simple, and it has therefore been frequently employed in Brain MR Image Segmentation (B-MRI-Se). Because the GMM is an image histogram-based model, it ignores the spatial relationship between nearby pixels, making it particularly susceptible to noise [7].

In this article, a standard GMM model merged with HMRF is developed by integrating the spatial correlation between neighbour pixels using a basic patch metric with the parameters optimized using the EM approach. Validate the proposed strategy by synthetic and real-world information and match it to alternative approaches, SS was the first approach for segmenting the brain from the skull and NBC intracranial structures in brain image analysis. It's made to deal with huge variances in brain shape and size, as well as the challenges that come with head MRI and the near proximity of brain tissues to NBC. The MSP is then detected in MRI human head images using the CF technique. Based on the discovered MSP, the Left Hemispheres (LH) and Right Hemispheres (RH) are divided. Finally, the automatic segmentation of the CCS in MRI images is performed using the GMM-HMRF-EM model. According to the GMM-HMRF-EM model, the energy matrix enhances the spatial features of the segmentation while decreasing the PV layer thickness, bringing it closer to the theoretical anatomical limit.

The following part is segmented as Briefly summaries related subject investigations in Section 2. In Section 3, the explanation about the proposed method. In Section 4, the suggested technique's performance is assessed using experimental data and compared to that of other comparable segmentation algorithms. A review of potential research directions closes Section 5.

II. LITRATURE SURVEY

Otsu, Bitplane, and the Adaptive Fast Marching Method (FMM) [8] suggested for automated brain, scalp, and skull segegrtaed from MRI. Three primary processes were designed in the research are (1) Preprocessing, (2) Segmentation, And (3) Classification. In the first Otsu technique, the brain structure determines a kind of each slice, and the head area is segregated by removing its backdrop. Then, the Bitplane method is used to divide the certain and doubtful regions. Ultimately, it suggests a categorization strategy based on the Adaptive FMM. This method is examined and compared to other approaches using the BrainWeb and Neurodevelopmental MRI datasets. On BrainWeb and Neuro-developmental MRI databases, the Dice Averages for brain, scalp, and skull segmentation have been enhanced.

A GM and WM thinning method for MRI head segmentation [9]. The model provides a novel segmentation method for obtaining exact cranial tissue layer thicknesses necessary for Diffuse Optical Tomography (DOT) data processing. Following the traditional Freesurfer GM and WM segmentation, the scalp was segregated as the initial stage in the algorithm. The lowering process involves regularly removing the outermost layer of

International Journal on Recent and Innovation Trends in Computing and Communication
ISSN: 2321-8169 Volume: 11 Issue: 11s
DOI: https://doi.org/10.17762/ijritcc.v11i11s.8092
***Article Received:** 20 June 2023 **Revised:** 22 August 2023 **Accepted:** 08 September 2023*

voxels until the desired amount of lowering stages is obtained. Finally, the iso2mesh toolbox's surface smoothing (Smoothbinvol) and 3-D volume filling (fillholes3d) approaches were used. The Root Mean Square (RMS) scalp thickness error is 1.60 mm, the skull thickness error is 1.96 mm, and the summed scalp and skull thickness fault is 1.49 mm with the suggested approach. Then, a segmentation measuring scale was used to assess the precision of tissue layer thicknesses in skull area where optodes are frequently inserted. The segmentation approach and assessment measure provided were assigned for increasing the detection rate of multimodal neuroimaging with DOT and coupled electroencephalography.

To developed an improved Convolutional Neural Network (CNN) U-net and Gaussian-Dirichlet Mixture Model (GMMD-U) for B-MRI-Se [10]. In this model, the possibility function is stated by following the Dirichlet distribution in which GMMD-U takes highly coarse connections into account. A modified U-net was utilised to address misclassification zones formed by GMMD or standard techniques, and GMMD employs in harvesting the brain tissue with a different intensity zone. The presented GMMD-U is designed to employ deep neural networks with statistical prototype segmentation algorithms. The proposed framework's performance on a publicly available brain MRI dataset is compared to the performance of other conventional algorithms, and the results suggest that the suggested scheme can consistently recognise brain tissue from MRIs. The segmentation method and evaluation measure shown here are tools for improving average Dice ratings. This framework might be effective in segmenting the brain tissue, so it could aid surgeons in diagnosing brain diseases.

To established a GMM and EM for brain MRI segmentation [11]. In the realm of medical image analysis, the B-MRI-Se into GM, WM, and CSF has gotten a lot of attention. The spatial relationship across pixels is neglected by the GMM since it is a histogram-based model, making it prone to noise. As a result, a new framework for adding spatial information into classic GMMs was created, in which each pixel is given its own prior depending on its neighbourhood features. The parameters of the recommended technique are calculated using EM. As simulated and clinical test MR images, the open datasets Brain-Web and Internet Brain Segmentation Repository (IBSR) is utilised, respectively. An overlap between segmentation results and ground-truth for each class is calculated using the segmentation accuracy ratio and the JS coefficient. On both synthetic and actual B-MRI-Se, the technique is shown to be effective in the segmentation problem.

Using K-means and GMM-EM to classify MRI abnormalities [12]. A lesion region may be automatically separated from the MRI scan images by utilizing both K-means and GMM-EM methods. The planned efforts are listed as follows: Preprocessing, feature extraction, and segmentation are all steps in the process. Initially, preprocessing procedures such as spatial normalisation, filtering, and smoothing were used to confirm that distinct images were in the same space. Images were magnitude based on the RMS throughout all participants to ensure that properties remained steady. The characteristics were then retrieved and normalised. To differentiate the tumor from other brain portion, K-means and GMM-EM were used. The evaluation characteristics of the algorithms were computed, and no significant differences between K-means and GMM-EM were discovered. Furthermore, the size of the lesion has minimal influence on the sensitivity and accuracy of any method.

In [13] created a CNN for B-MRI-Se automatically. MR brain images were automatically partitioned into a range of tissue categories using a CNN. To guarantee that the technique delivers correct segmental details as well as spatial constancy, the system receives inter-data for each voxel utilizing a variety of patch lengths and multiple convolution kernel values. The method relies on training data rather than explicit characteristics to learn to recognise the information that is critical for classification. The method just needs a single anatomical MR scan image. Five separate datasets were subjected to the segregation method. For each data set, the approach calculated the total DS for all segregated tissue classifications. The datasets used were NeoBrainS12 and MRBrainS13. Assessment measures such as the DS and the RMS are some of the examples.

A histogram technique and an adaptive region expansion method developed for segmenting 3D MRI images of the skull, scalp, and brain [14]. This model was developed for doctors use automated segmentation of 3D MRI images of the skull, scalp, and brain to help in the diagnosis of a range infections and traumas. Three post-processing adjustments were offered [15]: a one-of-a-kind alteration of the prior knowledge to eliminate segmentation bias; explicit partial volume classes; and an LV-MRF-based framework for sulci and gyri augmentation. Experiments using an advanced digital phantom, BrainWeb data, and data from the Alzheimer's Disease Neuroimaging Initiative (ADNI) show statistical significant progress in Dice scores and PV assessment, as well as enhanced width forecasting conformity, when compared to three well-established techniques.

III. PROPOSED METHODOLOGY

Due to variances in structure and volume, distortion, INU, PVE, MRI's limited resolution, with an exceeding architecture of the gyrifications, instant segmentation of cerebral cortex thickness from MRI images is difficult. In this research, an automated brain segmentation approach based on the cerebral cortex is presented for segmenting brain areas from axial and coronal MRI of human head scans. SS, BHS and CCS are the

International Journal on Recent and Innovation Trends in Computing and Communication
ISSN: 2321-8169 Volume: 11 Issue: 11s
DOI: https://doi.org/10.17762/ijritcc.v11i11s.8092
***Article Received:** 20 June 2023 **Revised:** 22 August 2023 **Accepted:** 08 September 2023*

three primary processes in the suggested technique. Further, in Step 1 involves removing NBC with a CTS-BEM. In step 2, a basic BHS approach is used to identify CF in MRI human head images. Based on the identified MSP, the LH and RH are segregated. Finally, add improvements to a probabilistic CCS framework such prior data modification to reduce segmentation bias, specified PVE and a GMM-HMRF-EM based segmentation model that varies locally. The suggested GMM-HMRF-EM algorithm's energy matrix enhances the segmentation's topological properties and decreases the PV layer thickness, bringing it closer to the theoretical anatomical limit. Fig. 1 shows proposed architecture of GMM-HMRF-EM.

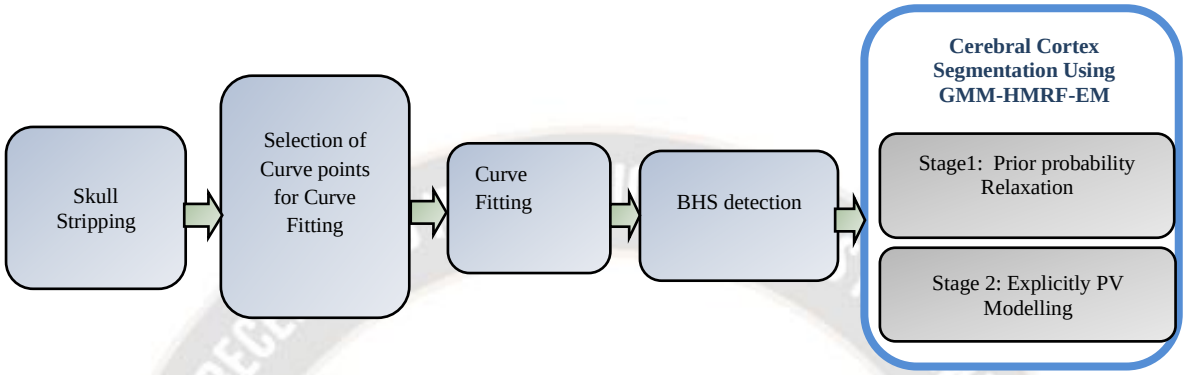

Figure 1. Proposed architecture of cerebral cortex segmentation

A. Skull stripping (SS)

A recent work [16] used a significant image quality enrichment approach based on a gamma adjustment developed using a classic research to increase the intensity of the brain image. The ideal gamma value to alter an image's overall intensity is determined using this gamma correction method. The disparity-improved images are then turned to binary images by the image down-sampling utilising square wave interpretation (SWI) [17]. As a consequence, the input brain lobes is pre-processed for quality enrichment and pattern classification at each step of this proposed technique.

Phase 1: Brain Extraction from Middle Slices

The brain region in the centre slice of an MRI head image exists as a specific Largest Linked Component (LCC). It makes capturing the Brain Mask (BM) of the principal layer in the brain capacity descriptive. It may be used to acquire cerebral segments from another after determining the BM for the centre slice. Image toning, morphological approaches, crude brain choosing, and fine brain border demarcation utilising a contour methodology are all part of the "brain extraction from centre slices" process.

For examination, the primary segment of the brain function is obtained. The LCC is a cerebral area that may be located in the brain capacity's inner regions. As a consequence, all of the CCs in g_E are labelled as the corrode images g_E using a run-length encoding technique to determine the LCC. This leads in labelling method in which all linked areas in g_E will be allocated a unique label. The specified g_{LCC} is dilated with O3 to fix the brain cells discarded in the erosion method. This approach utilizes a Structuring Element (SE) of dimension O3 for structural degradation and elongation operations.

There might be some huge gaps in the g_D. To create the holed-filled image g_{HD}, the huge holes in g_D are filled via a hole-filling method. g_{HD} is dilatable with O3 to generate the Rough Brain Mask g_{RBM}, as illustrated in Eqn. (1). Because it is often impossible to recover the original form of objects that have been dilated with SEs of equal or smaller size, the Rough Brain Mask (RBM) is calculated using Eqn. (1)

$$g_{RBM} = g_{HD} \oplus O_3 \tag{1}$$

where $\oplus$ is a dilation operator used to sum up the pixels to the object edges of an image. Eqn (2) selects the RB region using the g_{RBM}

$$g_{RB} = \begin{cases} f(x,y) \; if \; g_{RBM}(x,y) = 1 \\ 0 \; else \end{cases} \tag{2}$$

Smoothing is necessary before using the brain boundary detection by contouring approach to decrease noise and suppress spurious edges around the brain borders. By eliminating undesirable NBC pixels, the smoothing enhances the brain border while reducing the number of internal transects within the brain margin. A circular mean filtering with radius r is used to filter the information within a matrix form with edges having 2* r + 1.

After recognising all of the CCs in an image, the area labelling procedure assigns each CC a unique label. The first CC's pixel is designated 1, the second's is labelled 2, etc. CCs

International Journal on Recent and Innovation Trends in Computing and Communication
ISSN: 2321-8169 Volume: 11 Issue: 11s
DOI: https://doi.org/10.17762/ijritcc.v11i11s.8092
***Article Received:** 20 June 2023 **Revised:** 22 August 2023 **Accepted:** 08 September 2023*

will be intersected with g_{RBM} using Eqn. (3) can be recognised to create the coarse BM of the residual portions.

$$CC \cap g_{MC} \neq \emptyset \quad (3)$$

The CC s will either slightly or totally intersect with marker circle g_{MC} are decided as brain areas, while the others are omitted.

This algorithm proceeds above and down in the brain segment to capture the cerebral areas in the lower and higher levels after detecting the brain area in the centre slice. Next to the BM, the g_{MC} RBM is constructed. Equation (4) is then used to compute the Percentage of Overlap (PO) between the present g_{MC} and BM. A higher proportion of PO indicates that the g_{RBM} is comparable to the preceding neighbouring BM in form and is not related to NBC. If the brain slices have weak margins, the g_{RBM} may contain numerous interconnected non brain areas, resulting in a lower PO score. The morphological degradation procedure is used to separate these related NBC. Owing to the presence of fragile borders between the brain and NBC, the deterioration process frequently fails to separate the linked areas.

For those slices, the preceding BM is utilised as g_{RBM} . The g_{RBM} is then elongated by O (3) to restore brain pixels rejected in the degradation process, or the current rough BM may be somewhat larger than the previous BM if g_{RBM} is created using the prior BM.

$$PO(g_{RBM}, BM) = \frac{T(g_{RBM} \cap BM)}{T(g_{RBM})} * 100 \quad (4)$$

The maximum quantity of pixels in image X is $T(X)$. g_{RB} is chosen using Eqn. (2) after getting the g_{RBM}. It's smoothed out even further to create a Soft Rough Brain image g_{SRB}. The Fine Brain Boundary image g_{FBB} is drawn by outlining contour lines on g_{SRB} by the contour approach. The CCs in the Holes Filled brain boundary image g_{HFBB} that overlaps with g_{MC} are retrieved from the fine BM g_{FBM} once the holes in the g_{FBB} have been populated. By propagating one slice at a time from the centre slice to the lower slices, then from the lower slices to the middle slices, this method generates the BM for all portions. The brain segmentation findings of a 3D brain capacity are constructed after reviewing all of the 2D slices.

B. Brain Hemisphere Segmentation (BHS)

The inter-hemispheric edge is a circular-plane rather than a vertical column, because the brain will not perfectly symmetric. As a result, the curved MSP must be discovered in order to divide the LH, RH, Left Cerebral Hemispheres (LCH) and Right Cerebral Hemispheres (RCH) for brain asymmetry examinations.

Curve Points Selection (CPS): The CP is readily recognised when the neocortex is recovered from the source B-MRI utilising the MSP area, which divides the human brain into two CH. The MSP region is identified as a Region of Interest (ROI) and placed in the image's centre to choose curve nodes using this technique.

The identified ROI is transformed to binary code for CF using the technique of sample binarization employing a SWI described in recent work [17], because binary images are simpler to read than image pixels. After the pixels in the frame have been transformed to binary code, the dark/dark grey pixels in the SE are changed to black pixels, and these black pixels in the ROI are identified as CP.

When there is no black pixel in the binary representation of the selected ROI, the suggested approach employs three points (Begin, centre, and finish points) for curve fitting. The MSP is determined by fitting the appropriate CP with an II order polynomial CF method.

Curve Fitting (CF): A procedure to create a curve that matches a group of samples as closely as possible. The polynomial least squares method is the most prevalent strategy. It is a mathematical approach for determining which polynomial equations' coefficients best suit a collection of (x, y) statistics. Generic class of a quadric of $degree\ j$ will be represented by Equation (5).

$$y = a_0 + a_1 x + a_2 x^2 + \cdots . + a_j x^j = a_0 + \sum_{k=1}^{j} a_k\, x^k \quad (5)$$

. The $N - th$ order quadrilateral that better matches $N + 1$ data samples, for example.

Where $a0, \ldots, ak$ are correlations, x and j is a sample and polynomial stage respectively. In a polynomial variable, the reliant component y is written as a polynomial in the non-reliable variable x. The dependent element y is represented as a quadratic in the non-reliable variable x in a quadratic integer. The variables $a0, \ldots, ak$ may be used to forecast the results of y for each x of the optimal size, suggesting that there should be as minimal difference as possible between real y values and the quadratic equation's anticipated y properties. Moreover, the exponential phase should always be smaller than the number of instances for best matching.

As a consequences, the $N - th$ order polynomial should best matches the $N + 1$ data samples. The 1st order quadratic fits any two endpoints on a straight line with different x coordinates (degree N=1, number of sample 2), whereas the II order polynomial covers a curve with at least 3 parameters (degree N=1, number of sample 2). When the number of samples is smaller than N+1, it is predicted that the result will be infinite.

International Journal on Recent and Innovation Trends in Computing and Communication
ISSN: 2321-8169 Volume: 11 Issue: 11s
DOI: https://doi.org/10.17762/ijritcc.v11i11s.8092
***Article Received:** 20 June 2023 **Revised:** 22 August 2023 **Accepted:** 08 September 2023*

A CF method that identifies three samples from the CPS stage is detailed, with a II order polynomial being particularly well choice for CF. It's written as an Eqn. (6)

$$y_i = a_0 + a_1 x_i + a_2 x_i^2 \quad (6)$$

The data samples are x_i and y_i and the number of CP is $= 1, \ldots, n$. Solving the following matrix form yields the constants a_0, $a_1$and a_2 to a II order polynomial degree.

$$\begin{bmatrix} n & \sum x_i & \sum x_i^2 \\ \sum x_i & \sum x_1^2 & \sum x_i^3 \\ \sum x_i^2 & \sum x_i^3 & \sum x_i^4 \end{bmatrix} \begin{bmatrix} a_0 \\ a_1 \\ a_2 \end{bmatrix} = \begin{bmatrix} \sum y_i \\ \sum x_i y_i \\ \sum x_i^2 y_i \end{bmatrix} \quad (7)$$

No. of. CP is denoted by n, and the sum of all x values is denoted by $\sum x$ in the preceding Eqn. (7). The addiction of sum of all x and y values is denoted by $\sum xy$, and so on. The derived coefficients a 0,a 1,and a (2) are changed in equation to anticipate the values of y_i for each x_i (7). Fitting the curve with the CP x_i and projected y_i parameters yields the MSP.

C. Cerebral Cortex Segmentation (CCS)

The PACCS framework is presented in this section by altering prior data modification to eliminate the segregation biases, an emergence of explicit and a model by using a locally variable GMM-HMRF-EM model.

Stage 1: Prior Probability Relaxation

The EM approach is widely recognised for convergent to local maxima. The consistent certainty forces the EM process to a logical solution in the ML approach, rendering it highly susceptible to distortion and INU. Earlier directed ML approaches, on the other hand, may result in an inaccurate solution in areas with significant anatomical diversity, since the prior probability for the predicted class may be too close to 0 for the EM to converge to the desired result. It can also slant segmentation in the template's favour, potentially hiding anatomical differences. Suggestions for modifying the prior probability at each convergence of the EM algorithm should be anatomically consistent. The prototype parameters Φ_y grow closer to the actual answer as the EM method accumulates.

Stage 2: Explicit PV Modelling

It's a typical assumption in PV segmentation that when two tissues mix in a voxel, all mixing proportions are equally possible. PV probability is a collection of mixed Gaussians in the centre of the two clear categories that represents all conceivable tissue fractions within a voxel. The density of all four PV Gaussian classes may be matched by a single Gaussian with a moderate risk (one for D'Agostino-Pearson normality test) in brain imaging and for the signal-to-noise ratio and contrast-to-noise ratio values of current Devices.

The prior certainity, RMS, and deviation for the 8 classes model are termed by the letters $\pi_{ik}, \mu_k \; and \; \sigma_k$ respectively, with the superscript $*$ indicating that they belong to the 8 class model. For two mixed classes, the beginning mean, standard deviation, and priors must be calculated from the data, while the six pure classes retain their original values. Under the presumption of Gaussian distributed classes on log-transformed information, the preliminary combined class Gaussian specifications can be simulated by a mixel scattering, with mean equivalent to the arithmetic weighted aggregate of its composing class factors weighted by each group's mean fractional information.

Thus,

$$\mu_{\frac{j}{k}} = \Gamma_{\frac{j}{k}} \; \mu j + (1 - \Gamma_{\frac{j}{k}}) \mu_k \quad (8)$$

The average Fractional Content (FC) for classes j and k is $\Gamma_{\frac{j}{k}}$ for all voxels with $FC \in [0,1]$ where $\mathrm{FC} = \frac{\mu_j - y_i}{\mu_j - \mu_k}$ and $y_i = y_i - \Sigma_j c_j \phi_j (x_i)$ is the image sensitivity corrected for INU. Finding the mean mixing vector $t = [\alpha, 1-\alpha]$ in the model and using it as a weighting factor for all PV containing voxels is comparable to this. Using the same mixel model, the starting value of the mixed class deviation is determined. If the mixed class variance is just reliant on his constituent courses, the original estimate is as follows:

$$\left(\sigma_{\frac{j}{k}}^2\right)^* = \Gamma_{\frac{j}{k}}^2 \sigma_j^2 + \left(1 - \Gamma_{\frac{j}{k}}\right)^2 \sigma_k^2 \quad (9)$$

The segmentation robustness is hampered by Gaussians that must be incorporated into the PV model because no prior is available for the PV site. The presented technique solves this problem by integrating data from the six-class model with patient-specific geographical atlases to create an ad hoc mixed-class prior. In instances, the combined groups is obtained from the normalized geometric mean of its component tissue probabilities p_{ij} and p_{ij} consistent across all labels due to the multiplicative character of the probability.

$$\pi^*_{i\left(\frac{j}{k}\right)} = \frac{\sqrt{p_{ij} p_{ik}}}{0.5} \frac{1}{\Pi_i} \quad (10)$$

With Π_i is a Normalization variable across overall labels (see Fig. 2). In the labels, use $\pi_{ik} = \frac{p_{ik}}{\Pi i}$.. With a value of 1 for $p_{ik} = p_{ij} = 0.5 \; and \; 0$ for either p_{ik} or p_{ij}, the normalised arithmetic mean reflects how close p_{ik} and p_{ij} are to having equal proportions in each constituent tissues. Keep in mind, however, that $\pi_{i\left(\frac{j}{k}\right)}$ is merely a geometrical conversion needed to construct priors for the mixed class, not a measurement of PV

International Journal on Recent and Innovation Trends in Computing and Communication
ISSN: 2321-8169 Volume: 11 Issue: 11s
DOI: https://doi.org/10.17762/ijritcc.v11i11s.8092
***Article Received:** 20 June 2023 **Revised:** 22 August 2023 **Accepted:** 08 September 2023*

quantity. To begin a new step of the EM operation, type $p_{ik} = \pi_{ik}$.

In the EM method, the value of $X*$ is identified to reduce the maximum posterior energy.

$$X^* = \underset{X\epsilon x}{\operatorname{argmin}}\{|U(Y|X,\theta) + U(X)\} \quad (11)$$

When Y and θ are given, the probability energy (also known as unitary potential) is calculated.

$$U(Y|X,\theta) = \sum_i U(y_i|x_i,\theta) = \sum[\frac{(y_i-\mu_{x_i})^2}{2\sigma^2} + In\ \sigma_{x_i}] \quad (12)$$

The prior energy function is $U(X)$ (also known as pairwise potential).

$$U(X) = \sum_{c\epsilon C} V_c(X) \quad (13)$$

The clique potential is represented by $V_c(X)$, while the set of all possible cliques is represented by C. Assume that in the image domain, each pixel has no more than four neighbours: the pixels in its four-neighborhood. On pairs of neighbouring pixels, the clique potential is defined as follows:

$$V_c(x_i, x_j) = \frac{1}{2}(1\text{-}I_{x_i,x_j}), \quad (14)$$

Where

$$I_{x_i,x_j} = \begin{cases} 0 & \text{if } x_i \neq x_j \\ 1 & \text{if } x_i = x_j \end{cases} \quad (15)$$

The constant coefficient $1/2$ in Eq. (14) can be substituted with a variable coefficient.

To solve (1), an iterative algorithm is devised:

To begin, have a starting estimate $X^{(0)}$, which can come from the EM algorithm's prior loop.

1. Conditionally, $X^{(k)}$, for all $1 \leq i \leq N$, find

$$x_i^{(k+1)} = \underset{i\epsilon L}{\operatorname{argmin}}\{U(y_i|l) + \sum_{j\epsilon N_i} V_c(l, x_j^{(k)})\}. \quad (16)$$

2. Step 2 should be repeated until $U(Y|X,\Theta) + U(X)$ stops changing or a maximum k is reached.

Consider that each individual region's intensity distribution follows a Gaussian distribution with parameters $\theta_{x_i} = (\mu_{x_i}, \sigma_{x_i})$ However, this is a very strong hypothesis that is insufficient to represent the intricacy of real-life intensity distributions, particularly for items having multimodal representations In contrast to a single Gaussian distribution, and the GMM is far more powerful for modelling complicated distributions [18]. Parameters can be used to represent a GMM with g components:

$$\theta_l = \{(\mu_l, 1, \sigma_1, 1, w_{l,g})\} \quad (17)$$

Here, the GMM now has a weighted probability

$$G_{mix}(z;\theta_l) = \sum_{c=1}^{g} w_{l,c} G(z;\mu_{l,c},\sigma_{l,c}). \quad (18)$$

The EM-M-step algorithm's now becomes a GMM fitting issue, as stated in Section 2. The GMM fitting problem can alternatively be solved using an EM algorithm. In the E-step, determine which Gaussian component the data belongs to; in the M-step, recompute the GMM parameters. To increase the accuracy of the classification scheme even more, utilise the EM technique to estimate the included model parameters throughout the iteration, which is often employed to tackle the 'incomplete-data' problem. EM estimates converge locally to ML estimates under certain acceptable circumstances. The essential parameters for the HMRF- PVE model are really the mean vector and covariance matrix of each main tissue type l, type ℓ , that $\theta_l = \{\mu_l, \psi_l\}$, To utilise the EM approach, first estimate the missing information z given the current estimate, then use it to generate the whole data set y, z; finally, predict the new by maximising the complete-data log probability expectation.

The formalised EM algorithm is as follows:

Begin with the initial estimate $\theta^{(0)}$

Calculate a conditional expectation in the E-step as follows:

$$(\theta|\theta^{(t)}) = \varepsilon[\log P(y,z|\theta)|y,\theta^{(t)}] \quad (19)$$

The M-step increase $Q(\theta|\theta^{(t)})$ to determine the next estimate

$$\theta^{(i+1)} = arg\max_{\theta} Q(\theta|\theta^{(t)}). \quad (20)$$

Again, Repeat from E-step, Let $\theta^{(t+1)} \rightarrow \theta^{(t)(t)}$

When the EM method is used to the PVE HMRF model, the Q-function may be calculated as follows:

$$\begin{aligned} Q &= \varepsilon\{\log[P(y|z,\theta)P(z|\theta)]|y;\theta^{(t)}\} \\ &= \varepsilon\{[\log P(y|z,\theta) + \log P(z|\theta)]|y;\theta^{(t)}\} \\ &= \varepsilon\{[\sum_{i\epsilon S} \log P(\overrightarrow{y_i}|\overrightarrow{z_i},\theta) + \log P(z)]|y;\theta^{(t)} \\ &= \varepsilon\{\sum_{i\epsilon S} \log P(\overrightarrow{y_i}|\overrightarrow{z_i},\theta)|y;\theta^{(t)}\} + C \\ &= \sum_{i\epsilon S}\int_{\overrightarrow{z_i}} \log P(\overrightarrow{y_i}|\overrightarrow{z_i},\theta)P(\overrightarrow{z_i}|y;\theta^{(t)}) + C \end{aligned} \quad (21)$$

From Equation (21), it is difficult to compute or optimise with regard to since it requires an integration over all possible $\overrightarrow{z_i}$. As a result, a simplified approach is taken in which we use the partial volume proportion of tissue type ℓ at each voxel I to approximate the posterior probability of this voxel discretely being classified as that tissue $x_i = \ell$ given its neighbouring locations $x_{\mathcal{N}}$ and intensity $\overrightarrow{y_i}$; that is, $\forall \ell \in \mathcal{L}$

International Journal on Recent and Innovation Trends in Computing and Communication
ISSN: 2321-8169 Volume: 11 Issue: 11s
DOI: https://doi.org/10.17762/ijritcc.v11i11s.8092
***Article Received:** 20 June 2023 **Revised:** 22 August 2023 **Accepted:** 08 September 2023*

$$P\left(x_i = \ell \middle| \overrightarrow{y_i}, x_{\mathcal{N}_i}\right) \backsimeq z_{i\ell}, \tag{22}$$

Apply the EM technique for discrete image segmentation to estimate the parameters using this approximation. To put it another way, use an estimated Q-function:

$$\hat{Q} = \sum_{i\epsilon S} \sum_{x_{i\epsilon \mathcal{L}}} \log P(\overrightarrow{y_i} | x_i | y; \theta^{(t)}) + C, \tag{23}$$

x_i is the class label for pixel i and h is the collection of all possible labels. Mathematically

$$P\left(x_i | y; \theta^{(t)}\right) = \frac{P(y|x_i;\theta^{(g(t)})P(x_i)}{P(y)} \tag{24}$$

Given all of the requirements and assumptions, this is a costly calculation. As a result, to make the computation possible, make the following approximation:

$$P\left(x_i | y; \theta^{(t)}\right) \approx P\left(x_i \middle| \overrightarrow{y_i}, x_{\mathcal{N}_i}; \theta^{(t)}\right), \tag{25}$$

This is just the posterior probability of x_i based on its neighbours $x_{\mathcal{N}_i}$ and $\overrightarrow{y_i}$. Such an estimate is valid since the impact of the complete image's values on the label of the present pixel is conveyed through the influence of its particular level and the labelling setup of its neighbours.

For simplicity, it can be phrased as $P\left(x_i = \ell \middle| \overrightarrow{y_i}, x_{\mathcal{N}_i}; \theta^{(t)}\right)$ *as* $P^{(t)}(\ell | \overrightarrow{y_i})$.

$P\left(x_i | y; \theta^{(t)}\right)$ in Equation (26) has been replaced with the aforementioned approximation, and the approximation has been used.

$$\hat{Q} = \sum_{i\epsilon S} \sum_{i\epsilon \mathcal{L}} P^{(t)}(\ell | \overrightarrow{y_i} | \ell, \theta) + C$$
$$= \sum_{i\epsilon S} \sum_{i\epsilon \mathcal{L}} -P^{(t)}(\ell | y_i) \frac{1}{2} [\log|\psi_\ell| + (\overrightarrow{y_i} - \mu_\ell)^T \psi_\ell^{-1} (\overrightarrow{y_i} - \mu_\ell) + C'] + C, \tag{26}$$

IV. RESULTS AND DISCUSSION

In this paper, a segmentation approach is devised for the cerebral cortex that is particularly suited for it. This section evaluates the segmentation's ability to estimate cortical thickness directly on real data. The proposed and current segmentation techniques were evaluated using T1weighted brain images from the dataset. NBC are eliminated from the input brain slices during the preprocessing step, and then CF is utilized to perform hemisphere segmentation. The Precision, Recall, Specificity, JS, and DS scores were created for quantitative analysis because this dataset is the only one with hand-stripped distinction of brain lobes. The segmentation techniques are implemented in MATLAB.

A. Research Database

18 section of T1- density image was collected using the IBSR of the Centre for Morphometric Analysis (CMA) at the General Hospital Corporation (available online at http://www.cma.mgh.harvard.edu/ibsr/). 128 two-dimensional consecutive coronal sections at $256 * 256$ pixel width and a 1.5 mm slice girth are included in each volume. These MRI scanned images come from people of all ages, including children and the elderly. The IBSR also records how trained specialists manually separate (actual truth or gold grade) BM and identify brain areas. This dataset included images with poor contrast in several volumes. Torsten Rohlfing [21] has released these Images into the public domain. There are two distinct formats for the Images. Include data in CMA format ($ID * .img$) and Analyze format ($ID\ ana.img$). CMA image files come with an ASCII-readable 'description file' ($ID.info$) that comprises information like data dimensionality, size, spatial resolutions, orientation, and so forth. This information should enough for Image data display. For segmentation files, the 'Native CMA' ($ID * .otl$) outline format and a full volume in analysis format are also available.

The CMA.otl format is covered in depth further down. In the filled analysis formats, the fill code specifies how many structures were segregated. The shift from code to structure is covered in another appendix below. In addition, the segmentations are given in "trinary" format. In Analyze format files, the voxel value has been transformed from code-to-structure codes into the essential tissue types: background, CSF, GM, and WM. The codes are translated to the integers 0, 1, 2, and 3 as stated in the $file\ tr\_CMA\_to\_3$.

B. Experimental Analysis

The JS, DS, Precision, Recall, and Specificity between the input and the segregated Image are computed to evaluate the performance of the suggested technique. Equation [19-20] is used to compute the JS index (27).

$$J(S_1, S_2) = \frac{|S_1 \cap S_2|}{|S_1 \cup S_2|} \tag{27}$$

Equation (28) gives the DS

$$D(S_1, S_2) = \frac{2|S_1 \cap S_2|}{|S_1| + |S_2|} \tag{28}$$

where S_1 is the aggregate No. of. Image pixels obtained using the recommended method, and S_2 is the aggregate No. of. Image pixels obtained using intensity data (gold standard). The categorization of the suggested segmentation technique is based on the accuracy, recall, and specificity of the segmentation findings.

Precision is termed as a percentage of correctly categorised positive samples. This metric's estimation may be expressed as an equation (29),

$$Precision = \frac{TP}{FP + TP} \tag{29}$$

International Journal on Recent and Innovation Trends in Computing and Communication
ISSN: 2321-8169 Volume: 11 Issue: 11s
DOI: https://doi.org/10.17762/ijritcc.v11i11s.8092
***Article Received:** 20 June 2023 **Revised:** 22 August 2023 **Accepted:** 08 September 2023*

The term recall refers to the positive samples that have been assigned to the total number of positive samples, which may be calculated using the equation below (30),

$$Specificity = \frac{TN}{FP+TN} \quad (30)$$

Where, TP and FP stand for True Positive and False Positive, respectively, and it is known as the number of voxels categorized as brain tissue properly and wrongly using the suggested method. True negative and false negative refer to the voxels range properly with wrongly categorized as NBC by the indicated approach.

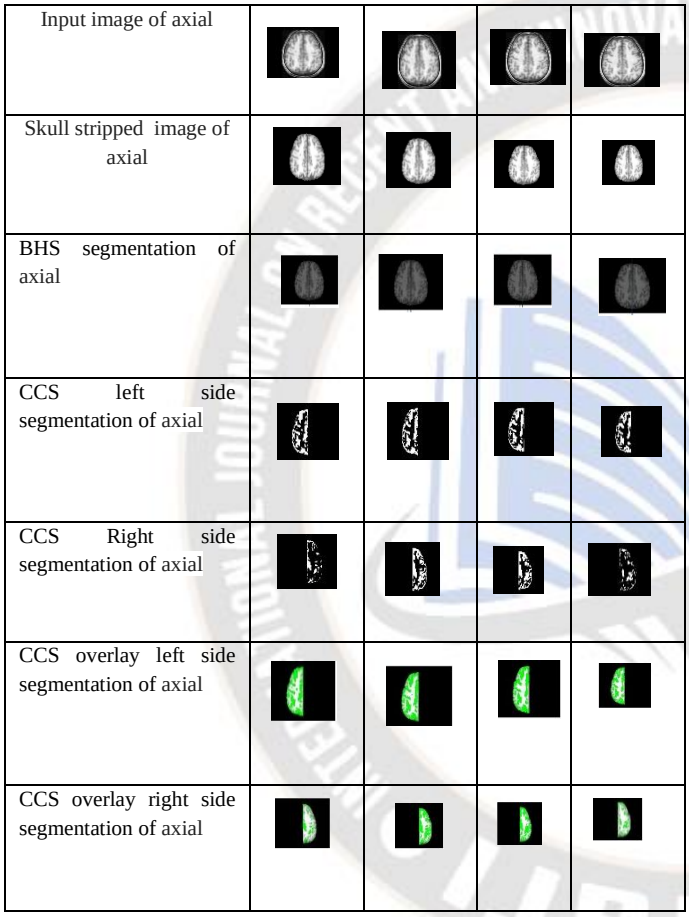

Figure 3. Results of LV-MRF MRF BASED CC segmentation in T1 weighted images (Axial class)

Fig. 3 depicts the findings of axial images in relation to four IBSR images. The input image is shown in the 1st row, the skull stripped images are shown in the 2nd row, and the BHS segmentation is shown in the 3rd row with regard to both side images. The 4th and 5th rows, respectively, exhibit the segregated results of CCS with LV-MRF for left and right side Images. In the 6th and 7th rows, the segmentation results of CCS with LV-MRF for overlay left side and overlay right side Images are displayed, respectively.

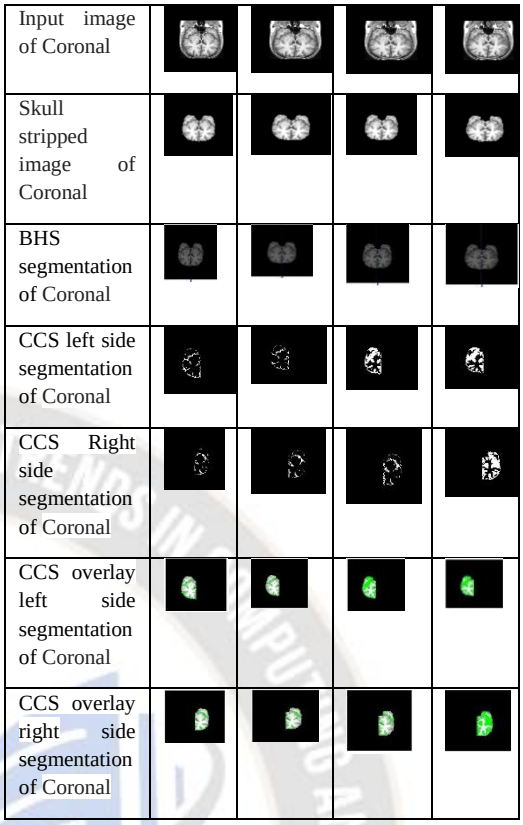

Figure 4. Results of LV-MRF based CC segmentation in T1 weighted images (coronal class)

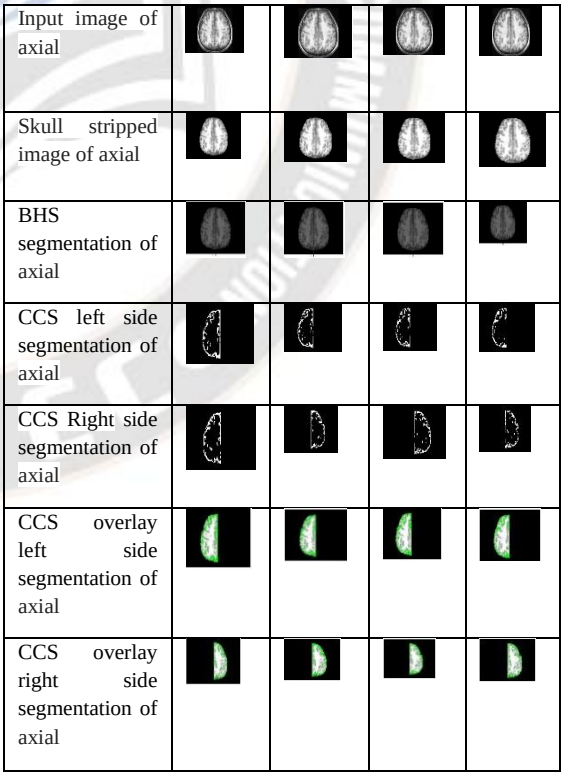

Figure 5. Results of GMM-HMRF-EM based CC segmentation in T1 weighted images (axial class)

International Journal on Recent and Innovation Trends in Computing and Communication
ISSN: 2321-8169 Volume: 11 Issue: 11s
DOI: https://doi.org/10.17762/ijritcc.v11i11s.8092
***Article Received:** 20 June 2023 **Revised:** 22 August 2023 **Accepted:** 08 September 2023*

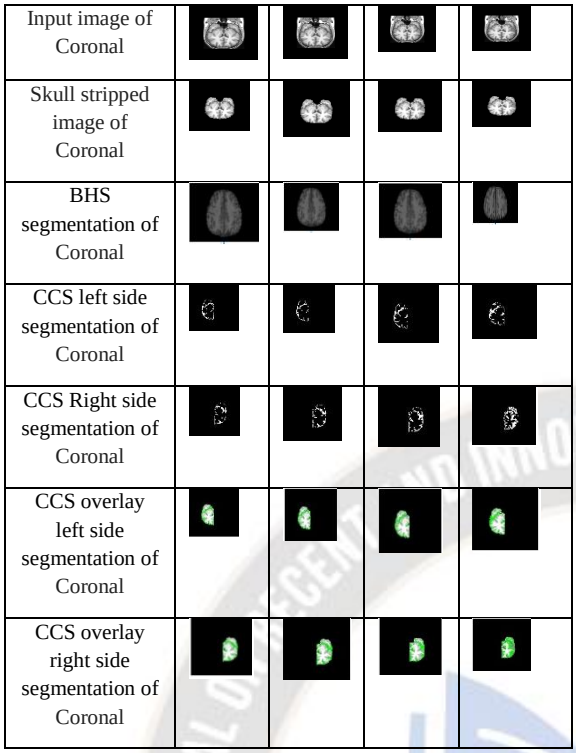

Figure 6. Results of GMM-HMRF-EM BASED CC segmentation in T1 weighted images (coronal class)

Fig. 4 shows the results of coronal images compared to four IBSR images. With reference to both side images, the input image is presented in the 1st row, the skull stripped images are shown in the 2nd row, and the BHS segmentation is shown in the 3rd row. The 4th and 5th rows, respectively, exhibit the segregated results of CCS with LV-MRF for left and right side Images. In the 6th and 7th rows, the segmentation results of CCS with LV-MRF for overlay left side and overlay right side images are displayed, respectively.

The findings of axial images in connection to four IBSR images are depicted in Fig. 5. With reference to both side images, the input image is presented in the 1st row, the skull stripped images are shown in the 2nd row, and the BHS segmentation is shown in the 3rd row. The 4rd and 5rd rows demonstrate the segmentation results of CCS utilizing GMM-HMRF-EM for the left and right side images, respectively. The 6th and 7th rows, respectively, exhibit the segmentation results of CCS with GMM-HMRF-EM for overlay left side and overlay right side images.

The findings of coronal Images are shown in Fig. 6 in contrast to four IBSR images. With reference to both side images, the input image is presented in the 1st row, the SS images are shown in the 2nd row, and the BHS segmentation is shown in the 3rd row. The 4th and 5th rows demonstrate the segmentation results of CCS utilizing GMM-HMRF-EM for the left and right side Images, respectively. The sixth and seventh rows, respectively, exhibit the segmentation results of CCS with GMM-HMRF-EM for overlay left side and overlay right side images. The values for the segmentation techniques were computed independently for different volumes such as Coronal Left Side, Coronal Right Side, Axial Left Side, and Axial Right Side, as shown in Table 1. Statistical Parametric Mapping 8 (SPM8) [22], Free Surfer [23], and LV-MRF are used to compare the findings.

Table 1. JS, DS, Precision, Recall, Specificity measures by the proposed segmentation and existing segmentation for dataset

Algorithm	Volume	Precision	Recall	Specificity	JS	DS
LV-MRF	Coronal Left side	0.604058	0.455894	0.970920	0.419644	0.483344
	Coronal Right side	0.608918	0.456726	0.971104	0.422492	0.482980
	Axial Left Side	0.582398	0.396499	0.962161	0.402496	0.411192
	Axial Right Side	0.596100	0.370749	0.965094	0.406733	0.404637
SPM8	Coronal Left side	0.605580	0.577360	0.976540	0.559644	0.512436
	Coronal Right side	0.609850	0.575450	0.977230	0.565648	0.523664
	Axial Left Side	0.612330	0.581436	0.974221	0.549624	0.585266
	Axial Right Side	0.713558	0.653736	0.979611	0.554463	0.536644
FREE SURFER	Coronal Left side	0.612336	0.865790	0.979566	0.602330	0.695607
	Coronal Right side	0.606565	0.706660	0.979565	0.576565	0.635321
	Axial Left Side	0.753342	0.676593	0.980120	0.597050	0.596653
	Axial Right Side	0.754530	0.728660	0.986542	0.586662	0.586651

International Journal on Recent and Innovation Trends in Computing and Communication
ISSN: 2321-8169 Volume: 11 Issue: 11s
DOI: https://doi.org/10.17762/ijritcc.v11i11s.8092
***Article Received:** 20 June 2023 **Revised:** 22 August 2023 **Accepted:** 08 September 2023*

GMM-HMRF-EM	Coronal Left side	0.633033	0.931133	0.989254	0.632793	0.740187
	Coronal Right side	0.667273	0.959080	0.990555	0.600946	0.706059
	Axial Left Side	0.836673	0.738119	0.988258	0.674308	0.600977
	Axial Right Side	0.894530	0.741331	0.989542	0.691447	0.626154

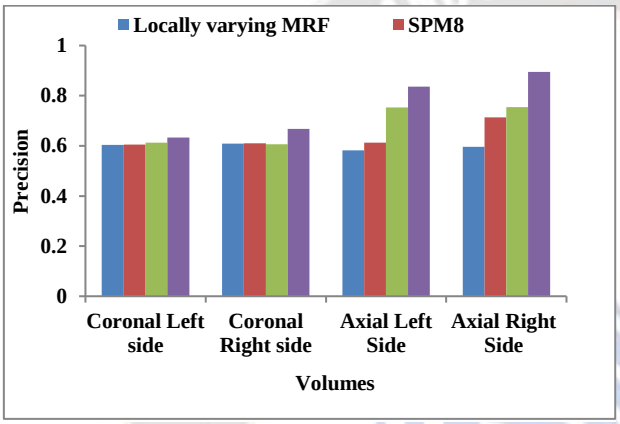

Figure 7. Precision Results Comparison of Segmentation Methods

Fig. 7 shows the precision outcomes for the comparison of segmentation methods in y axis and four volumes in x-axis. From the results it concludes that the proposed GMM-HMRF-EM with respect to Coronal Left side, Coronal Right side, Axial Left Side, and Axial Right Side gives highest precision results of 0.633033, 0.667273, 0.836673, and 0.894530, whereas existing LV-MRF, SPM8, and Free Surfer gives reduced precision value of 0.596100, 0.713558, and 0.754530 for Axial Right Side (Refer Table 1).

Fig. 8 shows the recall results comparison of segmentation methods in the y axis and four volumes in x-axis. From the results it concludes that the proposed GMM-HMRF-EM with respect to Coronal Left side, Coronal Right side, Axial Left Side, and Axial Right Side gives highest recall results of 0.931133, 0.959080, 0.738119, and 0.741331, whereas existing LV-MRF, SPM8, and Free Surfer gives reduced recall value of 0.455894, 0.577360, and 0.865790 for Coronal Left side (Refer Table 1).

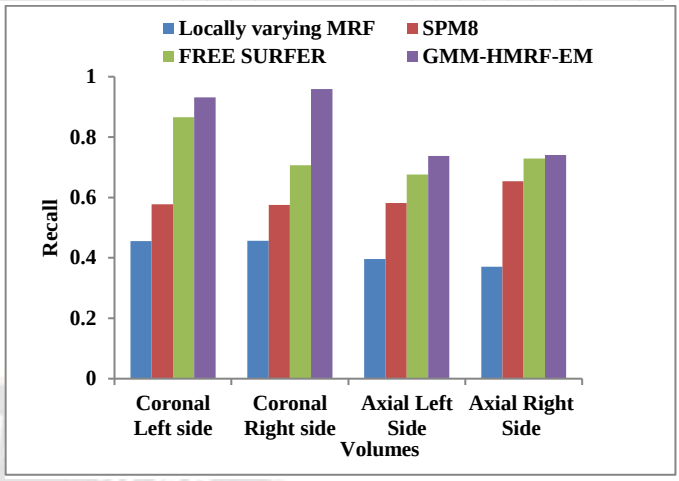

Figure 8. Recall Results Comparison of Segmentation Methods

Fig. 9 shows the specificity results comparison of segmentation methods in the y axis and four volumes in x-axis. From the results it concludes that the proposed GMM-HMRF-EM with respect to Coronal Left side, Coronal Right side, Axial Left Side, and Axial Right Side gives highest specificity results of 0.989254, 0.990555, 0.988258, and 0.989542, whereas existing LV-MRF, SPM8, and Free Surfer gives reduced specificity value of 0.971104, 0.977230, and 0.979565 for Coronal Right side. Similarly, it also gives higher results for right side of segmentation also which is clearly discussed in table 1.

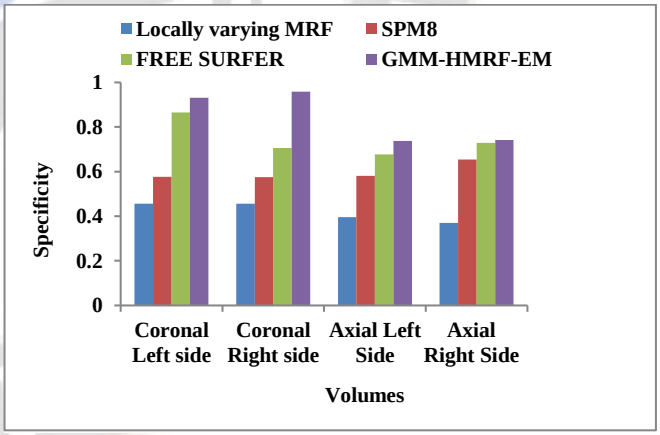

Figure 9. Specificity Results Comparison of Segmentation Methods

Fig. 10 shows the JS comparison of segmentation methods in the y axis and four volumes in x-axis. From the results it concludes that the proposed GMM-HMRF-EM with respect to Coronal Left side, Coronal Right side, Axial Left Side, and Axial Right Side gives highest JS results of 0.632793, 0.600946, 0.674308, and 0.691447, whereas existing LV-MRF, SPM8, and Free Surfer gives reduced JS value of 0.406733, 0.554463, and 0.586662 for Axial Right Side. Similarly, it also gives higher results for Axial Right Side of segmentation also which is clearly discussed in table 1.

International Journal on Recent and Innovation Trends in Computing and Communication
ISSN: 2321-8169 Volume: 11 Issue: 11s
DOI: https://doi.org/10.17762/ijritcc.v11i11s.8092
***Article Received:** 20 June 2023 **Revised:** 22 August 2023 **Accepted:** 08 September 2023*

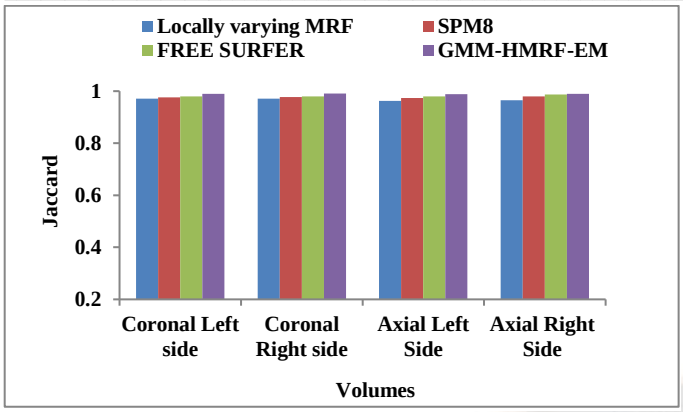

Figure 10. JS Comparison of Segmentation Methods

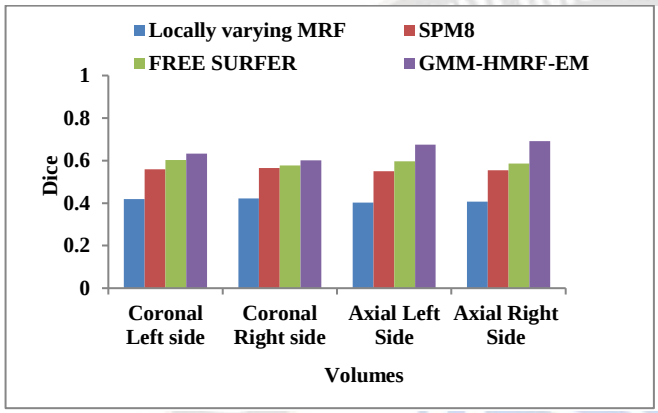

Figure 11. DS Comparison of Segmentation Methods

Fig. 11 shows the DS comparison of segmentation methods in the y axis and four volumes in x-axis. From the results it concludes that the proposed GMM-HMRF-EM with respect to Coronal Left side, Coronal Right side, Axial Left Side, and Axial Right Side gives highest DS results of 0.740187, 0.706059, 0.600977, and 0.626154, whereas existing LV-MRF, SPM8, and Free Surfer gives reduced DS value of 0.483344, 0.512436, and 0.695607 for Coronal Left side respectively which is referred in Table 1.

V. CONCLUSION AND FUTURE WORK

A unique segmentation technique is presented in this paper for determining the cerebral and cortical thickness estimation. The key contribution of this research may be broken down into three phases. To reduce the bias towards priors, a system that gradually relaxes and alters prior information in an anatomically appropriate manner is devised. The direct partial volume classes are introduced and their PV effect explicitly determined. Finally, energy is supplied to represent the inclusion of these additional classes using the GMM-HMRF-EM approach. In the final part, GMM is far more powerful than a single Gaussian distribution for representing complicated distributions. The state sequence of the HMRF model may be measured directly, but it may be indirectly approximated using data from the EM process. MATLAB is used to implement the algorithms. In PACCS segmentation trials, the suggested GMM-HMRF-EM algorithm outperforms the results of the LV-MRF method. The segregated results of the suggested work are significantly closer to the images than the existing technique. Since HMRF imposes more spatial limits on segregated regions than the current LV-MRF, it is an excellent choice. Precision, Recall, Specificity, JS, and DS metrics were derived for quantitative analysis. Based on the findings, it can be concluded that the suggested approach outperforms the LV-MRF in all criteria. CCS using three-dimensional structural brain-MRI is critical for assessing cortical tissue loss in illnesses like Alzheimer. It will be left as a project for the future. Researchers might develop hybrid approaches in the future to classify cerebral cortex sub-regions in MRI human head images by combining deep neural networks with past knowledge.

CONFLICT OF INTEREST

The authors declare no conflict of interest

ACKNOWLEDGEMENT

Funding, this work was supported by Science and Engineering Research Board (SERB) File No. EEQ/2016/000375, Department of Science and Technology, Government of India.

REFERENCES

[1] M.A. Balafar, “Gaussian mixture model based segmentation methods for brain MRI images,” Artificial Intelligence Review, vol.41, no.3, pp.429-439, 2014, doi:10.1007/s10462-012-9317-3.

[2] A. A. Pravitasari, Y. P. Hermanto, N. Iriawan, I. Irhamah, K. Fithriasari, S. W. Purnami and W. Ferriastuti, “MRI-based brain tumor segmentation using Gaussian mixture model with reversible jump Markov chain Monte Carlo algorithm,” In AIP Conference Proceedings, vol. 2194, no. 1, AIP Publishing, 2019, December, doi:10.1063/1.5139817 .

[3] W. Zheng, J.P. Kim, M. Kadbi, B. Movsas, I.J. Chetty and C.K. Glide-Hurst, “Magnetic resonance–based automatic air segmentation for generation of synthetic computed tomography scans in the head region,” International Journal of Radiation Oncology* Biology* Physics, vol.93, no.3, pp.497-506, 2015, doi:10.1016/j.ijrobp.2015.07.001.

[4] K. Keraudren, M. Kuklisova-Murgasova, V. Kyriakopoulou, C. Malamateniou, M. A. Rutherford, B. Kainz and D. Rueckert, “Automated fetal brain segmentation from 2D MRI slices for motion correction,” NeuroImage, vol. 101, pp. 633-643, 2014, doi:10.1016/j.neuroimage.2014.07.023.

[5] A. Jog, A. Hoopes, D. N. Greve, K. Van Leemput and B. Fischl, “PSACNN: Pulse sequence adaptive fast whole brain segmentation,” NeuroImage, vol. 199, pp. 553-569, 2019, doi:10.1016/j.neuroimage.2019.05.033.

[6] Q. Mahmood, A. Chodorowski, and M. Persson, “Automated MRI brain tissue segmentation based on mean shift and fuzzy c-

International Journal on Recent and Innovation Trends in Computing and Communication
ISSN: 2321-8169 Volume: 11 Issue: 11s
DOI: https://doi.org/10.17762/ijritcc.v11i11s.8092
***Article Received:** 20 June 2023 **Revised:** 22 August 2023 **Accepted:** 08 September 2023*

means using a priori tissue probability maps," Irbm, vol. 36, no. 3, pp. 185-196, 2015, doi:10.1016/j.irbm.2015.01.007.

[7] B. Lee, N. Yamanakkanavar, and J. Y. Choi, "Automatic segmentation of brain MRI using a novel patch-wise U-net deep architecture," Plos one, vol. 15, no. 8, pp. e0236493, 2020, doi:10.1371/journal.pone.0236493.

[8] T.A. Tuan, J.Y. Kim and P.T. Bao, "3D brain magnetic resonance imaging segmentation by using bitplane and adaptive fast marching," International Journal of Imaging Systems and Technology, vol.28, no.3, pp.223-230, 2018, doi:10.1002/ima.22273.

[9] K.L. Perdue and S.G. Diamond, "T1 magnetic resonance imaging head segmentation for diffuse optical tomography and electroencephalography", Journal of biomedical optics, vol.19, no.2, pp.1-8, 2014, doi:10.1117/1.JBO.19.2.026011.

[10] J. Lai, H. Zhu and X. Ling, "Segmentation of brain mr images by using fully convolutional network and gaussian mixture model with spatial constraints," Mathematical Problems in Engineering, 2019, doi:10.1155/2019/4625371.

[11] Y. Song, Z. Ji, Q. Sun, "An extension Gaussian mixture model for brain MRI segmentation," In 2014 36th Annual International Conference of the IEEE Engineering in Medicine and Biology Society (pp. 4711-4714). IEEE 2014, August, doi:10.1109/EMBC.2014.6944676.

[12] Kartika S. (2016). Analysis of "SystemC" design flow for FPGA implementation. International Journal of New Practices in Management and Engineering, 5(01), 01 - 07. Retrieved from http://ijnpme.org/index.php/IJNPME/article/view/41.

[13] J. Qiao, X. Cai, Q. Xiao, Z. Chen, P. Kulkarni, C. Ferris and S. Sridhar, "Data on MRI brain lesion segmentation using K-means and Gaussian Mixture Model-Expectation Maximization," Data in brief, vol. 27, 104628, 2019, doi:10.1016/j.dib.2019.104628.

[14] P. Moeskops, M. A. Viergever, A. M. Mendrik, L. S. De Vries, M. J. Benders and I. Išgum, "Automatic segmentation of MR brain images with a convolutional neural network," IEEE transactions on medical imaging, vol. 35, no. 5, pp. 1252-1261, 2016, doi:10.1109/TMI.2016.2548501.

[15] T. A. Tuan, J. Y. Kim and P. T. Bao, "Adaptive region growing for skull, brain, and scalp segmentation from 3d mri," Biomedical Engineering: Applications, Basis and Communications, vol. 31, no. 05, pp. 1950033, 2019, doi:10.4015/S1016237219500339.

[16] M. J. Cardoso, M. J. Clarkson, G. R. Ridgway, M. Modat, N. C. Fox, S. Ourselin and Alzheimer's Disease Neuroimaging Initiative. " LoAd: a locally adaptive cortical segmentation algorithm," NeuroImage, 56(3), 1386-1397, 2011, doi:10.1016/j.neuroimage.2011.02.013.

[17] Kim, H. ., Jeong, Y. ., Seo, S. ., Youn, J. ., & Lee, D. (2023). A Study on Radiant Heat Application to the Curing Process for Improvement of Free-Form Concrete Panel Productivity. International Journal of Intelligent Systems and Applications in Engineering, 11(4s), 157–164. Retrieved from https://ijisae.org/index.php/IJISAE/article/view/2583.

[18] K. Somasundaram and P. Kalavathi, "Medical image contrast enhancement based on gamma correction. Int J Knowl Manag e-learning, vol. 3, no. 1, pp. 15-18, 2011.

[19] K. Somasundaram and P. Kalavathi, "Medical image binarization using square wave representation," In International Conference on Logic, Information, Control and Computation, pp. 152-158, Berlin, Heidelberg: Springer Berlin Heidelberg, 2011, February, doi:10.1007/978-3-642-19263-0_19.

[20] Q. Wang, "GMM-based hidden Markov random field for color image and 3D volume segmentation," arXiv preprint arXiv:1212.4527, 2012, doi:10.48550/arXiv.1212.4527.

[21] P. Kalavathi and V. B. Surya Prasath, "Automatic segmentation of cerebral hemispheres in MR human head scans," International Journal of Imaging Systems and Technology, vol. 26, no. 1, pp. 15-23, 2016, doi:10.1002/ima.22152.

[22] K. Somasundaram and P. Kalavathi, "Contour-based brain segmentation method for magnetic resonance imaging human head scans," Journal of computer assisted tomography, vol. 37, no. 3, pp. 353-368, 2013, doi: 10.1097/RCT.0b013e3182888256.

[23] Luca Ferrari, Deep Learning Techniques for Natural Language Translation , Machine Learning Applications Conference Proceedings, Vol 2 2022.

[24] T. Rohlfing, "Image similarity and tissue overlaps as surrogates for image registration accuracy: widely used but unreliable," IEEE transactions on medical imaging, vol. 31, no. 2, pp. 153-163, 2011, doi:10.1109/TMI.2011.2163944.

[25] D. Izquierdo-Garcia, A. E. Hansen, S. Förster, D. Benoit, S. Schachoff, S. Fürst and C. Catana, "An SPM8-based approach for attenuation correction combining segmentation and nonrigid template formation: application to simultaneous PET/MR brain imaging," Journal of Nuclear Medicine, vol. 55, no. 11, pp. 1825-1830, 2014, doi:10.2967/jnumed.113.136341.

[26] L. Palumbo, P. Bosco, M. E. Fantacci, E. Ferrari, P. Oliva, G. Spera and A. Retico, "Evaluation of the intra-and inter-method agreement of brain MRI segmentation software packages: A comparison between SPM12 and FreeSurfer v6. 0.," Physica Medica, vol. 64, pp. 261-272, 2019, doi:10.1016/j.ejmp.2019.07.016.